Performance Comparison of 3D Printed Photoacoustic Gas Sensors and a Commercial Quartz Enhanced Photoacoustic Spectrometer

Utkarsh Dwivedi, *Member, IEEE,*Mark Donnachie, Metin Ilke, Ralf Bauer, Michael Lengden

***Abstract*— This paper presents a comparison of photoacoustic spectroscopy gas sensors manufactured using different 3D printers. The sensors have been designed with varying resonator diameters, 1 mm and 2mm, and lengths, 12.34 mm and 30 mm, and using two different microphones, an electret microphone and a MEMS microphone. The comparison showed little variation in sensor performance based on printer type or geometry. However, the MEMS microphone based sensors showed a factor of 2-3 improved Normalised Noise Equivalent Absorption (NNEA) performance as compared to sensors using the electret microphones. A commercial quartz enhanced photo-acoustic sensor was additionally tested and also showed a factor of 2-3 poorer NNEA performance as compared to the MEMS based, 3D printed photoacoustic sensors. Finally, a discussion is provided on the performance of the 3D printed cells used in this work and previous 3D printed PAS sensors.**

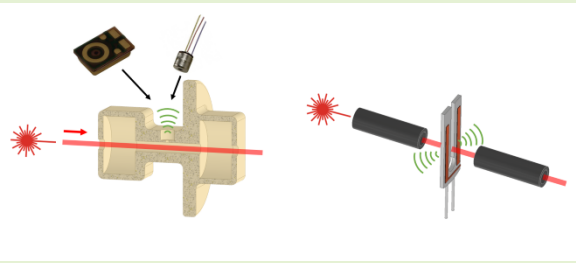

***Index Terms*— Photoacoustic sensors, gas sensing, 3D printing.**

I. Introduction

THE last 15 years have seen an ever increasing interest and research output in the use of photoacoustic spectroscopy (PAS) for high sensitivity spectroscopic gas measurements (parts-per-billion to trillion range). This is due to the advent of more stable mid-IR optical sources [1] and the development of more miniaturised and ruggedised photoacoustic sensors using novel acoustic transducers [2], [3], [4], integrated resonator designs [5], and novel manufacturing methodologies [6], [7], [8]. In 2014, we used early stage, expensive stereolithographic 3D printers to manufacture miniaturised resonant acoustic structures, coupled with micro-electromechanical systems (MEMS) microphones and fibre coupled optics, that had normalised noise equivalent absorption (NNEA) levels of the order of 10^{-9} W cm^{-1} Hz$^{-1/2}$ [9]. However, 3D printing technology and costs have developed significantly since this earlier work due to the increased commercial and consumer demand for μm resolution printers. This has seen printer costs reduce from in excess of ten thousand pounds to the few hundreds of pounds for a printer of similar quoted resolution performance.

This work was supported in part by the UK Engeineering and Physical Sciences Research Council under grant EP/K034758/1. For the purpose of open access, the authors have applied a Creative Commons Attriubutioni (CC BY) licence to any Author Accepted Manuscript version arising from this submission.

U. Dwivedi, M Donnachie, M Ilke, R Bauer and M Lengden are with the Department of Electronic and Electrical Engineering, University of Strathclyde, Glasgow,G1 1XW, UK e-mail: michael.lenden@strath.ac.uk.

In this paper, we present the performance characteristics of PAS sensors manufactured using two modern, commercially available printers; the Formlabs Form 3, aimed at commercial rapid prototyping, and the Anycubic Photon S, aimed at consumer 3D-printing. We begin this investigation by characterising the printing quality of these two printers through analysis of the surface roughness using a nanometer resolution stylus profiler (Section III). We then present the NNEA performance characteristics for a number of 3D printed sensors manufactured with longitudinal resonator designs of various resonator lengths and radii, fabricated with the two 3D printers *and two newly identified microphone types; a Knowles MEMS microphone on a flex-PCB (SPV08A0LR5H-1) and a Knowles electret microphone (FG-23742-D36), (Section V).* To aid this performance investigation we have also compared the 3D printed PAS sensors manufactured using these newly identified microphones with a commercial quartz tuning fork based PAS sensor as well as other research in 3D printed PAS sensor design.

The overall aim of this paper is therefore evidence the high level of performance achievable using 3D printed PAS sensors, and to provide a workflow for producing high quality, 3D printed resonant PAS cells that can be cheaply manufactured at low cost, and require little post-print construction or optical alignment.

II. Justification for Miniaturisation of PAS Sensors

Various methodologies have been used to improve the overall sensitivity of PAS, with the two most common being the development of acoustic resonators to amplify the generated acoustic wave, and the use of high power optical sources to impart more energy into the gas and thus generate higher thermo-acoustic modulation and increased signal levels. The increase in optical power can also be achieved by placing the PAS resonator within a laser cavity [10] or into a multi-path set-up with high reflectivity mirrors, e.g. a cavity ring-down set-up [11]. In this work, we have focussed on the miniaturisation of the acoustic resonator for signal amplification, and this section presents a detailed justification for miniaturisation in PAS.

For a standard cylindrical acoustic resonator there are longitudinal, radial and azimuthal resonant modes. The frequency of each mode, $f_{j,m,q}$, can be calculated using the equation

$$f_{j,m,q} = \frac{c_s}{2}\left[\left(\frac{\alpha_{j,m}}{R}\right)^2 + \left(\frac{q}{l}\right)^2\right]^{1/2} \quad (1)$$

where c_s is the speed of sound, l is the resonator length, R is the radius of the cylinder, j, m and q are non-negative integers referring to the eigenvalues of the radial, azimuthal and longitudinal modes respectively and $\alpha_{j,m}$ is the j^{th} zero of the derivative of the m^{th} Bessel function divided by π [12].

If we assume that each resonant mode has a high quality factor, Q, and is well separated, then the generated pressure wave for each mode, $p\left(f_{j,m,q}\right)$, in a cylindrical resonant PAS cell is described as

$$p\left(f_{j,m,q}\right) \approx \frac{\alpha C l P_L (\gamma - 1)}{f_{j,m,q} V} Q_{j,m,q} F K\left(f_{j,m,q}\right) \quad (2)$$

where α is the absorption co-efficient of the identified spectral feature of the target gas, C is the target gas concentration, P_L is the incident laser power, γ is the specific heat ratio of the target gas, V is the volume of the resonator, K is the microphone response and F is the overlap integral of the resonance and the optical heat source.

Typically, PAS resonators are designed to target the fundamental longitudinal resonant mode, i.e. $q = 1$, and $j = m = 0$, thus reducing equation (1) to

$$f_{1,0,0} = \frac{c_s}{2l} \quad (3)$$

Equations (2), and (3) highlight the geometrical requirements for designing a suitable resonator, with a resonator length at a user-defined resonant frequency and the reduction in volume to ensure a maximum possible generated acoustic pressure.

For longitudinal resonant cells, the generated pressure wave will be increased with a reduction in volume when one only considers the non-resonant excitation. Therefore, cells with a reduced radius increase the generated pressure wave. However, consideration also has to be given to the chosen length in order to operate at a chosen resonant frequency using equation 3. When also taking into account the Q-factor, which is affected by energy losses within the resonator (viscous and thermal dissipation inside the boundary layers at the smooth internal resonator surfaces; acoustic wave scattering at surface obstructions; flexibility of the chamber walls; and dissipation at the microphone diaphragm [12]), the generated pressure wave is proportional to

$$p\left(\omega_r\right) \propto \frac{\sqrt{l}}{R} \quad (4)$$

Therefore, a reduction in the cell length decreases the generated pressure wave, while a reduction in cell radius improves the generated pressure wave and overall sensitivity. However, any reduction in cell radius also leads to a smaller volume to surface area ratio, which ultimately reduces the quality factor of the resonance to a value of 1. Additionally the excitation laser beam needs to pass through the cell without obstruction, which sets a further limit to the minimum cell radius. There is therefore a limit to the reduction in volume that can be achieved before energy losses overcome any signal amplification.

The use of high resolution 3D printing technology allows cells of millimeter dimensions to be manufactured in a simple one step manufacturing process, but an understanding of surface quality is needed to ensure a suitable Q-factor can be achieved. Therefore, for 3D printed PAS sensors consideration has to be given to printer resolution and print surface roughness, which impacts on the minimum achievable cell radius, surface profile, and polymer stiffness. Consideration also has to be given to the ability to accurately couple an acoustic transducer to the resonator and to optically couple light into the resonant chamber, as the complexities and costs of coupling into smaller geometries may lead to increased optical loss at surfaces, or reduced ruggedness/miniaturisation through the requirement for additional beam shaping optics. In Section III we provide detailed surface roughness analysis of the two 3D printers used to manufacture our current PAS sensors.

III. 3D Printer Performance and Cell Manufacture

A. Printer Characteristics

In this work, we have investigated the performance of two current generation 3D printers: a Formlabs Form 3 and an Anycubic Photon S; and compared them with the original 3D printed PAS cell manufactured using an EnvisionTEC Aureus Plus. The specifications for these printers are shown in table I. Each of these printers operate with the same basic principle: the polymerisation of a liquid polymer using UV light. However, the technologies used by each device are different.

The printer performance has been analysed by measuring the surface roughness of prints using a stylus contact line profiler (Tenkor AlphaStep; measurement range of 3 mm with 5 μm diameter tip and a height resolution of less than 1 nm). Unfortunately, the high recommissioning cost of the Aureus printer used in earlier work has not allowed the manufacture of new prints with this printer, which did not allow test samples to be printed for surface profile analysis. For the two

TABLE I
COMPARISON OF 3D PRINTER PARAMETERS, AS SUPPLIED BY THE MANUFACTURERS AT TIME OF PUBLICATION.

Printer	Manufacturer	x-y resolution (μm)	Voxel (z) Resolution (μm)	Build Envelope (mm)	Resin
Aureus Plus	EnvisionTEC	43	25-35	60 x 45 x 80	R11 Acrylic Resin
Form 3	Formlabs	25	25-300	145 x 145 x 185	HTM 140
Photon S	Anycubic	47	10-100	115 x 65 x 155	Maroon UV Cured Resin

printers we used resins available from the manufacturers; a high temperature deflection resin, HTM140, - Formlabs, and a resin with little detail other than the colour, 'maroon', Photon S.

For the Formlabs and Photon S printers, 3 mm x 3mm x 3mm polymer blocks have been printed in two different orientations: one block from each printer printed in the x-y plane ('flat'); one block from each printer printed at an angle of 30^o with respect to the y-axis ('angled'). The angled print has been oriented such that there will be a step structure in the yz-plane of the block due to the printer's z-resolution, but there should be no structure in the xz-plane. All printed blocks were scanned along both the x- and y-axes to identify any pixelation in the print (from the flat blocks), and any major step structure (from the angled blocks).

Figure 1 (a) shows the stylus profile from the flat HTM140 and 'maroon' blocks, with the surface scan over a 3 mm length in the x-direction. For the HTM140 block, the difference between the maximum and minimum block height, Δd, was measured to be around 10.46 μm in both the x- and y-direction scans. The standard deviation of deflection across the 3 mm measurement range, which we define as the surface roughness, has been measured as 1.4 μm. Both these values are well below the quoted 25 μm XY resolution, and the print does not show any real surface structure. The results for the surface roughness of the flat 'maroon' block, from the Anycubic printer, show a smaller level of surface roughness, with a Δd of 2.7 μm and a standard deviation of 0.74 μm. However, the surface roughness contains a periodic structure not visible in the HTM140 polymer. This periodic structure clearly identifies a pixelation pattern in the 'maroon' polymer matched to the 47 μm pixel size of the LCD screen used in the printer.

Figure 1 (b) and (c) show stylus profiles of the angled blocks along the y-direction (b) and the x-direction (c). It is clear that the Formlabs printer does not produce any 'digitised' layering or stepping, despite the print angle. In fact, the stylus deflection distance Δd is still only 5-10 μm. The assumed reasoning behind this improved performance is the use of a semi-transparent resin that allows the print process to illuminate and cure layers printed during prior steps and smoothing out the print. This then assumes there is an element of inherent post-process coating to the semi-cured resin throughout the print. The overall conclusion for the Formlabs is that the surface roughness between the flat and angled prints is very similar, and the surface roughness is lower than the quoted pixel resolution. For the Anycubic printer, figure 1 (b) shows clear layer steps and individual pixels within each step. Each step is approximately 25-30 μm in height, and the stepping occurs every 600 μm scanned along the block. This stepping should not occur in the xz-plane, which is perpendicular to the angled print axis, but figure 1 (c) shows that there is also stepping in the xz-plane. However, this stepping is much less pronounced and is probably due to misalignment of the stylus scan axis, which is aligned manually with respect to the print angle layers. It is, however, clear that the Anycubic printer, using a non-transparent polymer, produces a pixelated print when both flat and angled prints are used and a stepped roughness in the angled print, neither of which are apparent in the HTM140 polymer print from the Formlabs printer.

B. 3D Printed Cell Manufacture

For this work, cells have been designed and manufactured with a resonator length of 12.34 mm and radii of both 1 mm and 2 mm, and a cell was also designed and manufactured with a 30 mm resonator length and 2 mm radii. For each resonator design, cells were produced for the two different microphone types, and typical designs for the two different microphones are shown in figure 2. The electret microphone is a cylindrical, canister shaped microphone with pre-soldered wire leads. Therefore, an empty slot with a diameter of 2.8 mm is added above the resonator centre to ensure an accurate alignment when the microphone is placed in the sensor. In this case, the acoustic coupling duct has a 0.3 mm diameter and 0.2 mm height. The MEMS microphone is located on a flexible-PCB with an alignment hole, allowing simple connection between the acoustic coupling hole (0.3 mm diameter and 0.1 mm height) and the microphone, and the use of a thinner coupling height.

The resonator lengths were chosen to investigate the performance of sensors operating at resonance frequencies at the upper and lower ranges of the chosen microphones. The two radii were chosen to understand sensor performance due to the assumed increased pressure for reduced radius and the counteracting increased surface losses. Radii smaller than 1 mm were not investigated as the sensor is designed to use simple fibre coupled optical collimators for beam propagation.

The main design parameters follow a specific set of criteria. Initially, the resonator length and diameter are defined. Buffer volumes are then added for noise suppression, and these have a diameter of 6 times the resonator diameter and a length dimension of half the resonator length. Gas inlet and outlet ports are added with diameters of 4.3 mm to allow connection with 1/4" stainless steel or PTFE pipes. Finally, optical coupling holes are added of equal diameter to the designed resonator. This allows the same optical set-up to be used to characterise each sensor. In our previous work, the optical coupling ports were designed for use with a either a fibre coupled GRIN lens [6] or using 2 mm thick windows [13]. In this work, the optical coupling ports remained open

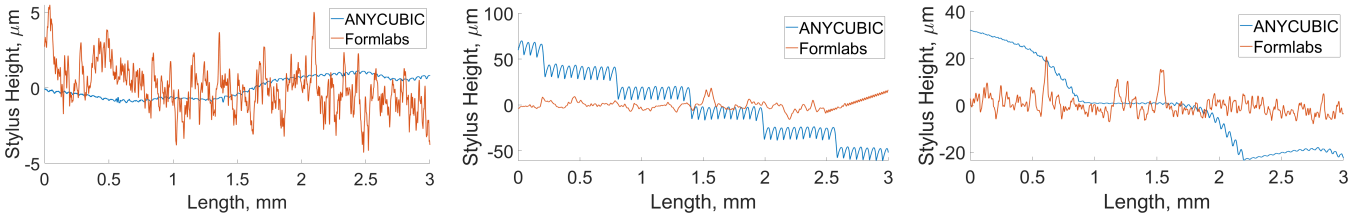

(a) Flat Block (b) Across Grain - y-plane (c) Parallel to Grain - x-plane

Fig. 1. Stylus profiles of 3D printed blocks of dimensions 3 mm x 3 mm x 3 mm from the Formlabs and Anycubic printers. (a) shows a typical profile from blocks printed in the x-y plane of the printer. (b) shows a typical profile in the y-axis of the block when the block is printed at 30^o with respect to the y-axis. (c) shows a typical profile in the x-axis of the block when the block is printed at 30^o with respect to the y-axis.

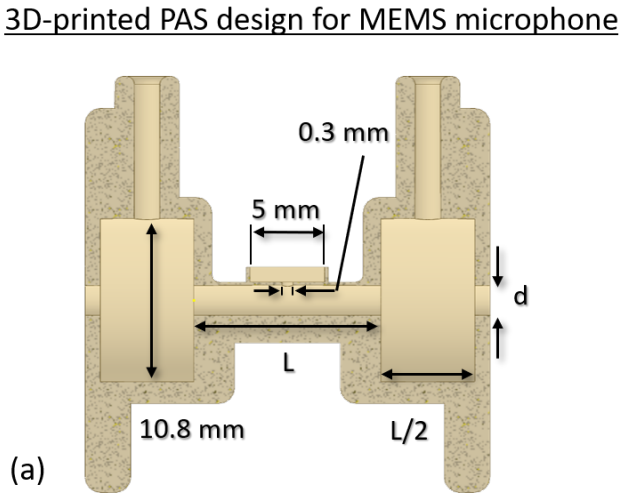

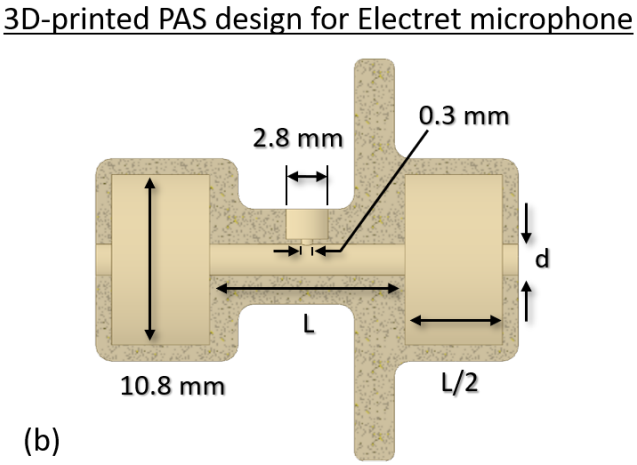

Fig. 2. Typical PAS cell design using both a MEMS acoustic coupling port (a) and an electret, canister based coupling port (b). The length and diameter of the resonators have been varied throughout this research. We define the length as L, which defines the buffer length as L/2, and the resonator and optical coupling port diameter as d (parameters given in Table II). All units are mm.

to ensure accurate optical power measurements within the resonator for the NNEA measurements.

Each cell is printed at an angle of 30° with respect to the y-axis of the printer. The print angle is required to reduce the force required to lift the print at each layer, which in principle

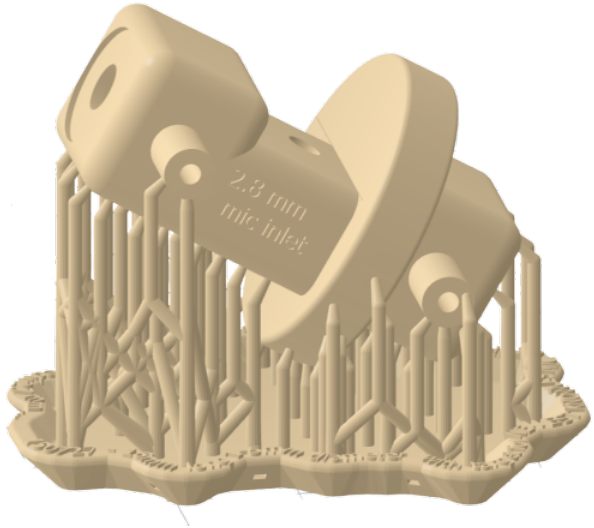

Fig. 3. Prepared design for printing with 30° to horizontal plane with supports

leads to a better print quality of the 3D print, and the angle also allows excess liquid polymer to flow through any cavities in the print. The design with added supports is shown in figure 3.

Once the cell is manufactured the microphone is aligned within the acoustic port of the sensor. To ensure microphone alignment, a photo-acoustic signal of atmospheric water vapour is monitored in real time using the experimental set-up shown in figure 5. The spectral feature of water vapour used during this monitoring process is at a wavelength of 1392.5 nm.

Figure 4 shows the frequency response of a PAS cell during different stages of microphone alignment and gluing: (1) pressure applied to push the microphone into the acoustic coupling port and microphone sealed in place with epoxy glue, (2) pressure applied but no epoxy, (3) neither epoxied nor pressure applied. As expected, when the microphone is fixed in place and glued the resonator produces the maximum acoustic signal. The gluing process typically doubles the generated acoustic signal as compared to when the microphone is neither fixed nor sealed.

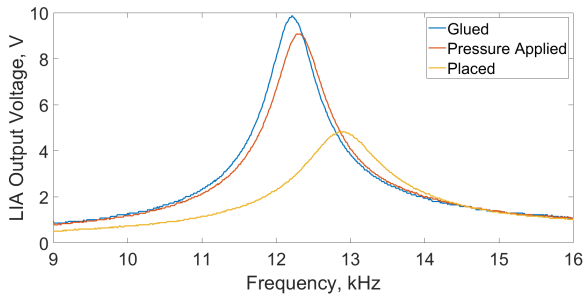

Fig. 4. Frequency characterisation of the same PAS cell during different phases of assembly. A MEMS microphone was used in this comparison.

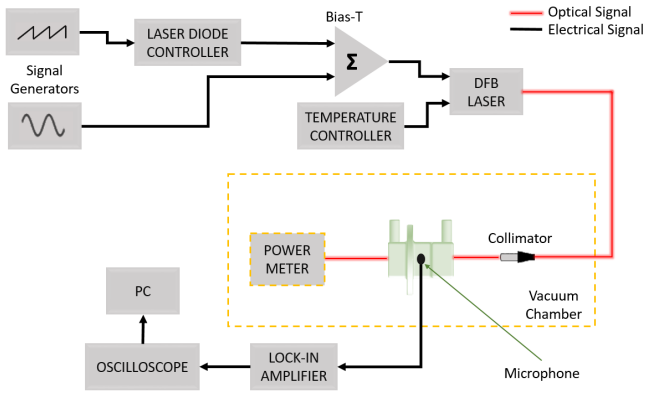

Fig. 5. Experimental set-up for the calculation of normalised noise equivalent absorption for the different 3D printed PAS cells.

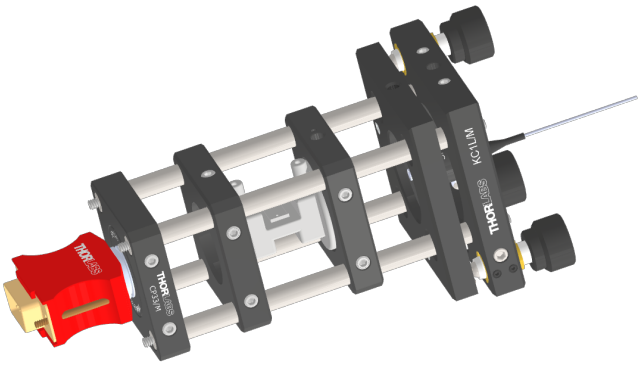

Fig. 6. Optical cage-mounting system for the optical components used to measure the signal performance on the 3D printed photoacoustic cells.

IV. Experimental Set-Up and Measurement Process

The experimental set-up used to evaluate the sensor performance based on NNEA calculations for each cell is shown in figure 5, where the NNEA provides an equivalent signal to noise ratio based around optical absorption rather than the concentration of a specific gas and thus allowing the SNR to be calculated for any absorption feature of any target gas and for any incident optical power. This is the same set-up as for the microphone alignment, except the sensor is now placed within a vacuum chamber to allow the use of calibrated gas mixtures within the PAS cell. The laser source is a fibre coupled distributed feedback laser (DFB), with a central wavelength of 1650.96 nm and a maximum output power of 4 mW. The laser's output wavelength is thermally tuned, using a Thorlabs TED 200 C thermoelectric current controller, to target the R(4) ro-vibrational transition of methane. A 5 Hz current ramp, generated via an Agilent 33210A 10 MHz Arbitrary Waveform Generator and a Thorlabs LDC 210C laser diode current controller, is applied to the DFB to fully interrogate the R(4) spectral feature. A high frequency sinusoidal current modulation is also applied to the laser, via a Bias-Tee, using a second Agilent 33210A 10 MHz Arbitrary Waveform Generator. The frequency and current amplitude of the sinusoidal modulation are chosen to match the measured resonant frequency for each individual PAS cell (table II), and to target a first harmonic modulation index, $m = \delta\nu/\gamma$, of 2, where $\delta\nu$ is the amplitude of the applied frequency modulation, and γ is the half-width of the absorption line-shape. Targeting m = 2 provides the highest tunable diode laser with wavelength modulation (TDLS-WM) first harmonic signal, and thus generating data with the maximum available signal to noise ratio/NNEA [14].

The light output from the optical fibre of the laser is collimated using a fibre coupled c-lens (Opneti), with a working distance of 50 mm and $1/e^2$ full-width of 1mm, located within a Thorlabs CP35 1" lens mount for optical cage mount systems. A S155C Thorlabs power-meter head is used to monitor the output power from the PAS cells to calculate the NNEA, as shown in figure 6.

The whole cage mounted optical rig is then located within a vacuum chamber, built around a 4-way stainless steel cross-piece with connectors for four CF-160 flanges. Two 9-pin miniature d-sub electronic feedthroughs allow electrical connections for the microphone and the power-meter, and two Swagelok 1/4 inch compression fittings are used as a bespoke optical fibre feed-through and a gas/vacuum feedthrough respectively.

The chamber is filled with a calibrated gas mixture of 1008 ppm methane with a nitrogen buffer gas (premixed gas, BOC) and the generated acoustic signals are fed into a Stanford SR830 lock-in amplifier (LIA). The magnitude of the first harmonic signal output from the LIA, R1f, was measured using a digital oscilloscope (TDS 3014B Textronix - 8 bit, 100 MHz bandwidth and 1.25 GS/s sampling rate), which outputs 10,000 data-points over the 5Hz time-period. A GPIB interface is used to record the oscilloscope signals onto a personal computer.

The process for the NNEA calculations requires three distinct steps. Firstly, the resonance frequency for the cell is obtained by measuring the R1f signal at frequency increments of 10 Hz over the resonance profile of the specific longitudinal resonance of the tested resonator and figure 4 shows a typical resonance plot. Secondly, the m = 2 value is obtained for the calculated resonance frequency by measuring the amplitude of the high frequency current modulation incremented in 1 mA steps until the maximum R1f output is found. Finally, the NNEA is calculated using the R1f measurement taken at

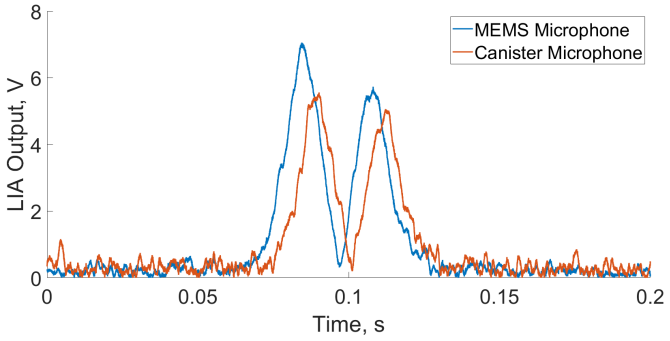

Fig. 7. Output response from the SR 830 lock-in amplifier for the 12.34 mm long, 2 mm diameter resonators using the MEMS and electret microphones. This time constant of the LIA was set to 300 μs, with a 24 db/oct low pass filter

resonance and m = 2 and the equation

$$NNEA = \frac{P_0 \alpha_{3\sigma}}{\sqrt{\Delta f_{LIA}}} \tag{5}$$

where P_0 is the incident power measured on the power meter and Δf_{LIA} is the frequency bandwidth of the LIA, set to 260 Hz, and $\alpha_{3\sigma}$, is the absorption calculated for a signal to noise ratio, SNR = 3. To obtain the value of $\alpha_{3\sigma}$ the following equation can be used

$$\alpha_{3\sigma} = \alpha_M \frac{\sigma_V * 3}{M_V} \tag{6}$$

where α_M is the known absorption for the 1008 ppm calibration gas (4.514 X 10^{-4} cm^{-1}), σ_V is the standard deviation of the noise signal, obtained by using a high-pass filter on the recovered R1f signal, and M_V is the measured voltage at line centre, obtained using a low-pass filter on the R1f. Figure 7 shows the R1f signals recorded for the 12.34 mm long, 2 mm radius PAS cells using the MEMS and electret microphones.

V. Results

The list of tested cells is given in table II. For reference, the longitudinal cell printed on the Aureus printer, which had a length of 10 mm and a diameter of 1.8 mm, had a NNEA of 4.5 x 10^{-9} W cm^{-1} $Hz^{-1/2}$. This original design therefore still outperforms all these newly printed sensors by at least a factor of 1.38. In the original work, a discontinued miniature MEMS microphone (Wolfson Microelectronics WM7131) was used as the acoustic sensor and the acoustic coupling port was of 0.75 mm diameter and 0.25 mm height, which implies a similar height of acoustic coupling duct but a much smaller diameter. Also, the resonator was 1.8 mm diameter to accommodate the incident laser beam from a fiber coupled gradient index (GRIN) collimators (Photop KFCS-A-900T1550-N-100-C-NN), which is similar to the 2 mm diameter resonators used here. The improved performance of the original design is minimal, and is probably due to the sealing of the optical coupling ports using GRIN lenses.

From table II it can be seen that the major contributor to cell performance is clearly the choice of acoustic transducer, as the MEMS transducers used in this work show similar performance to the original cell design with a MEMS transducer. Even though the quoted performance of the MEMS and electret transducers is similar, it is clear that the MEMS devices provide a factor of 2-3 better NNEA performance. The major difference between these types of microphone is the dimensions, with the electret device having an internal 1.5 mm air gap before the sensing membrane, whereas the MEMS packaging height is less than 0.9 mm in total including the PCB thickness of 0.285 mm. The MEMS device also has an acoustic port diameter of 0.25 mm, an order of magnitude lower than the 2.5 mm acoustic port for the electret device. As such, the total volume of air within the MEMS device is significantly smaller than for the electret microphone. In fact, the air volume within the electret device is comparable to the volume of the smallest designed acoustic resonators. The increased air volume of the electret sensor leads to the generation of a Helmholtz resonance in the acoustic coupling port and a loss in the acoustic energy coupled from the resonator. This assumption is further validated by the reduced Q-factor of the electret based sensors, and the higher drop in resonant frequency from the theoretically calculated values.

In terms of printer performance, both the Anycubic and Formlabs printed sensors using a MEMS microphone have a comparable NNEA to our original sensor, manufactured on a printer which has an order of magnitude higher cost.

Resonator diameter performance was tested using two resonators of the same length, 12.34 mm, but with different diameters, 1 and 2 mm. For both the Anycubic and Formlabs designs, the cell with a 1 mm diameter outperformed the 2 mm cell in terms of NNEA, thus highlighting that acoustic losses to surface roughness are not the most dominant factor when 3D printed cells are designed with a smaller, 1 mm radius.

Also of interest is the performance of the PAS cells with a 30 mm resonator length and a 2 mm diameter. For these cells, the overall Q-Factor is higher than for the shorter length cells. In fact, the 30 mm length resonator using an electret transducer has the highest performing NNEA of any electret transducer design. This is believed to be due to the increased volume of the resonator, as compared to the acoustic coupling duct in the electret microphone, reducing the effect of the Helmholtz resonance that leads to acoustic energy loss. This is further evidenced by the measured resonance of the 30 mm long electret based sensor having a percentage difference ($\%_{diff}$) of only 6 % with respect to the theoretical resonance, as compared to the $\%_{diff}$ of 14 % for the 12.34 mm long, 2 mm diameter electret PAS sensor. This improved acoustic coupling due to the increased resonator volume is also identified in the MEMS based sensors, where the $\%_{diff}$ of the resonant frequency for the 30 mm long resonator is 1.3 % as compared to 8 % for the 12.34 mm long, 2 mm diameter resonator. However, due to the lower acoustic coupling duct volume in the MEMS setup, this effect does not have such a major improvement on NNEA.

VI. QEPAS Comparison

To compare the 3D-printed PAS sensor performance to QEPAS, we have used a commercially available QEPAS sensor

TABLE II

LIST OF 3D PRINTED H-CELLS, WITH THE LENGTH AND RADIUS DIMENSIONS OF THE RESONATOR REGION, THE PRINTER AND POLYMER USED, AND THE CALCULATED NNEA VALUES.

Resonator Length (mm)	Resonator Diameter (mm)	Theoretical Resonance Frequency (Hz)	Resonance Frequency (Hz)		Q-Factor		NNEA ($Wcm^{-1}Hz^{-1/2}$)	
			AnyCubic	Formlabs	AnyCubic	Formlabs	AnyCubic ($x10^{-9}$)	Formlabs ($x10^{-9}$)
12.34	1	13742	12000	12800	1.46 (Electret)	6.4 (MEMS)	15.7 (Electret)	5.8 (MEMS)
12.34	2	13709	11700	12220	2.8 (Electret)	7.4 (MEMS)	19.8 (Electret)	7.67 (MEMS)
30	2	5555	5220	5480	6.96 (Electret)	10.06 (MEMS)	14.3 (Electret)	6.8 (MEMS)
”	”	”	5470	-	9.96 (MEMS)	-	6.2 (MEMS)	-

(Thorlabs - ADM01) while the same optical set-up shown in figure 5 is used. The QEPAS sensor is made up of a single, customised quartz tuning fork (QTF), with a 0.8 mm tine separation, and two micro-resonators, each with 1.6 mm diameter and 12.4 mm length. The sensor is packaged into a sealed chamber with a volume of 7 cm^3, which has two G 1/8 straight connectors for 6 mm gas tubing, and two BaF_2 windows for optical coupling through the acoustic sensor. The top flange of the chamber can be removed to allow easier alignment through a micro-resonator and tuning fork.

The combined micro-resonator/QTF sensor has a quoted resonant frequency of 12455 Hz and a Q-factor of $>$ 12000. This high Q-factor implies a much longer ring-down time of the QTF when excited at resonance. In the 3D printed sensing work, the laser is frequency scanned over the gas line of interest at 5 Hz, thus providing more physical information about the gas within the measurement volume, i.e. pressure or temperature. Such a scan rate is not possible in a QTF system due to the reduced damping and associated resonance ring-down times, and therefore the laser scan frequency has to be lower than 10 mHz to maximise the recovered signal. Also, the use of the two micro-resonators within the QEPAS system changes the acoustic signal generation methodology. In this case, the laser's high frequency sinusoidal modulation has to be at half the resonant frequency, and the LIA is set to recover the magnitude of the second harmonic signal, R2f.

The methodology for calculating the NNEA for the QEPAS sensor is the same as described in section IV, therefore the QEPAS sensor is operated at atmospheric pressure with a gas mixture of 1008 ppm methane with a nitrogen buffer. To ensure light passed through the 0.8 mm separation distance between the QTF tines, the same c-lens collimator used for the 3D printed sensor work was used here with a loss in optical power of only 0.1 mW (2 %) through the sensor. However, a 2-mirror arrangement was added to allow pitch and yaw alignment, whilst the QEPAS sensor was mounted on a Thorlabs PY005 5-axis stage. The final NNEA for the commercial QEPAS sensor was 12.7 x 10^{-9} W cm^{-1} $Hz^{-1/2}$, with figure 8 showing the R2f data recorded for 1008 ppm methane over the 10 mHz scan time and the filtering for the NNEA calculation. Therefore, the QEPAS system has almost 3 times poorer NNEA performance as compared to 3D printed sensors using MEMS microphones. The resonance frequency was found to be $\approx$ 12455.74 Hz as shown in figure 9.

There are various points of discussion that can be drawn from this comparison of QEPAS and miniaturised 3D printed PAS sensing. Firstly, the manufacturer's website does not pro-

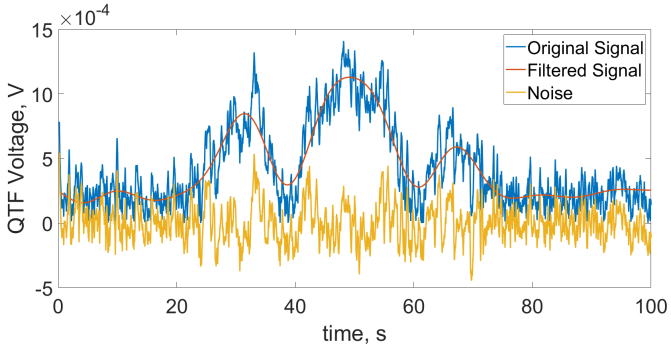

Fig. 8. Commercial QEPAS sensor output response using SR 830 lock-in amplifier set to 3 ms time constant and 24 dB/oct low pass filter. The figure shows the original data from the LIA, the 'signal' data obtained using a digital low-pass filter and the 'noise' data obtained using a digital high-pass filter. The two filtered signals are used for the NNEA calculation

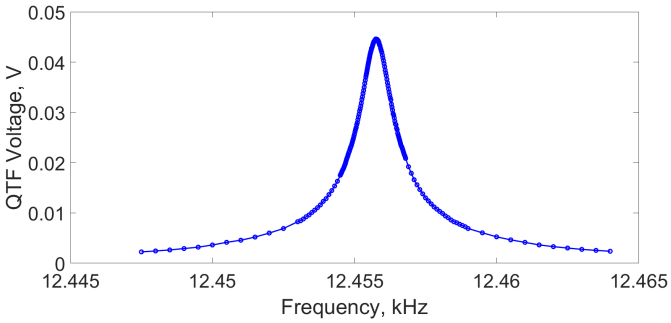

Fig. 9. Commercial QEPAS sensor output response as a function of frequency for 10 % methane.

vide an equivalent specification to the NNEA, and published QEPAS sensors have always shown similar performance to the 3D printed sensors developed in our work. Given the NNEA calculations in this paper have been performed using the same methodology, it is valid to assume the commercial-off-the-shelf sensor has a poorer NNEA. However, the QEPAS approach has certainly been proven with much higher performing NNEA values. Secondly, when using any wavelength modulation scheme for signal recovery we have always scanned the laser over a whole absorption profile, rather than locking the laser to the peak absorption. This allows the recovery of the whole absorption profile, thus providing more physical data than if only the absorption peak is measured. Due to the high Q-factor of the QTF this results in the requirement for a very slow current scan rate, and QTF based systems may show better performance when operated in a laser-

locked methodology using long LIA time-constants. Finally, the commercial QEPAS cell has a sample volume of 7 cm^3, which is much greater than the volumes of the 3D printed cells. This is because the QEPAS cell is housed within a stainless steel vessel with optical access via windows, which has two purposes: the ruggedization for the QTFs in a commericaial off the shelf system, and to allow the measurement of controlled gas samples. The PAS cells used in this paper were also housed within a stainless steel vessel, but this was to allow for characterisation of the PAS cells without the need to gas seal each PAS cell using optical coupling via windows or GRIN lenses. In our previous work, we have shown that the 3D printed PAS cells can be easily manufactured with sealed windows [13] and with fibre collimators [6], and this ensures that gas samples can be taken within closed volumes of less than 0.1 cm^3 (30 mm x 2 mm cell).

VII. Comparison with other 3D Printed PAS Sensors

The work of Zhang et al. [15] used a longitudinal resonant cell that has a 3D printed casing but with a central copper resonator section of length 40 mm and diameter of 4.5 mm. The sensor also has a reflector on one end to allow a double optical path through the copper resonator. The microphone used was an electret condenser device. Two NNEAs are quoted in the paper, 4.42 $\times$ 10^{-9} W cm^{-1} $Hz^{-1/2}$ and 2.27 $\times$ 10^{-9} W cm^{-1} $Hz^{-1/2}$, both of which are calculated using a 1σ minimum signal calculation. It is assumed that the latter NNEA is for an averaging time of 50 s, which was the time at which the minimum detectable absorption was calculated using an Allan Variance plot. If the former value is the calculated single-shot NNEA measurement, then the system performance is comparable to the work in this paper using an electret microphone. However, if the latter NNEA is used then the performance of their cells is similar to the performance of our MEMS based devices. The work of He et al. [16] used a 3D printed holder to allow gas access to a standard QTF sensor with stainless-steel micro-resonators, as used in the commercial QEPAS sensor. The total internal volume of this cell was 1.5 cm^3, and the 3D printed buffer volumes are used to suppress the flow noise of gas entering the cell. 5 mm long, 0.5 mm diameter stainless steel micro-resonators were used each side of the QTF, resulting in a total length of $\approx$ 11 mm, with the light entering the first micro-resonator via a 1.8 mm diameter fibre coupled GRIN lens. The quoted 3σ NNEA for this sensor is calculated to be 32.4 $\times$ 10^{-9} W cm^{-1} $Hz^{-1/2}$, which is poorer than the cells in this work. Niu and Song [17] used 3D printing to print two micro-resonators for a QTF PAS system, with lengths of 4.4 mm and diameters of 0.6 mm with a quoted 3σ NNEA was 15 $\times$ 10^{-9} W cm^{-1} $Hz^{-1/2}$.

The work of Rück et al. is of significant interest [18]. They use a much more complex 3D printing design with rotatable mounted Brewster windows ensuring minimal acoustic noise due to absorption into the optical coupling windows. Again, they have used a stainless steel tube as the resonator, with a length of 38.7 mm and a diameter of 3.95 mm, and have drilled a 1.2 mm diameter acoustic coupling port into the resonator. They also have an adaptor to allow the use of various acoustic transducers. The quoted NNEA is 2.1 $\times$ 10^{-9} W cm^{-1} $Hz^{-1/2}$ using a MEMS microphone, which is a factor of 2-3 higher than the performance of the cells in this work but at the cost of more complex manufacture.

It is assumed that 3D printed cells using metal inserts for the resonator are to ensure that acoustic losses at the surfaces are minimised. However, from the work shown in this paper it is clear that the quality of print surface roughness is high enough to ensure surface losses from full 3D printed resonators are similar to those with metal inserts, but without the requirement for further manufacture.

VIII. Conclusion

This paper has presented data for various geometries of longitudinally resonant, 3D printed photo-acoustic cells. We have shown that the three commercial printers used in the manufacturing process provide similar performance in terms of SNR for PAS detection, even for a printer providing surface structures of up to 30 μm. The use of PCB mounted MEMS microphones gave an improvement in NNEA compared to canister shaped electret microphones, due to the reduced coupling volume in the acoustic duct. A reduction in the resonator radius has additionally shown an improvement in the NNEA. However, for radii of 1 mm and lower this may come with a requirement for more complex beam shaping to ensure optimal coupling of the optical excitation beam throughout the resonator. Without this beam shaping there is a reduced overall performance due to the lower optical power coupled into the resonator, although this doesn't affect the NNEA. It is also clear that the increase in resonator length improves the Q-factor as the volume of the resonator increases as compared to the volume of the acoustic coupling duct (including the microphone). However, this does not always equate to an improved NNEA, due to the increased electronic noise at lower measurement frequency and the reduction in the magnitude of the pressure wave as the volume is increased. Finally, we have shown that the performance of a COTS QEPAS sensor is also poorer as compared to the performance of 3D printed sensors using MEMS acoustic transducers.

References

[1] F. Capasso, C. Gmachl, A. Tredicucci, A. L. Hutchinson, D. L. Sivco, and A. Y. Cho, "High performance quantum cascade lasers," *Opt. Photon. News*, vol. 10, no. 10, pp. 31–37, Oct 1999. [Online]. Available: http://www.optica-opn.org/abstract.cfm?URI=opn-10-10-31

[2] A. A. Kosterev, Y. A. Bakhirkin, R. F. Curl, and F. K. Tittel, "Quartz-enhanced photoacoustic spectroscopy," *Opt. Lett.*, vol. 27, no. 21, pp. 1902–1904, Nov 2002. [Online]. Available: http://opg.optica.org/ol/abstract.cfm?URI=ol-27-21-1902

[3] V. Koskinen, J. Fonsen, K. Roth, and J. Kauppinen, "Cantilever enhanced photoacoustic detection of carbon dioxide using a tunable diode laser source," *Applied Physics B*, vol. 86, no. 1, pp. 451–454, 2007.

[4] H. Wu, L. Dong, H. Zheng, Y. Yu, W. Ma, L. Zhang, W. Yin, L. Xiao, S. Jia, and F. K. Tittel, "Beat frequency quartz-enhanced photoacoustic spectroscopy for fast and calibration-free continuous trace-gas monitoring," *Nature Communications*, vol. 8, 2017.

[5] J. P. Waclawek, R. Lewicki, H. Moser, M. Brandstetter, F. K. Tittel, and B. Lendl, "Quartz-enhanced photoacoustic spectroscopy-based sensor system for sulfur dioxide detection using a cw dfb-qcl," *Applied Physics B*, vol. 117, no. 1, 2014.

[6] R. Bauer, G. Stewart, W. Johnstone, E. Boyd, and M. Lengden, "3d-printed miniature gas cell for photoacoustic spectroscopy of trace gases," *Opt. Lett.*, vol. 39, no. 16, pp. 4796–4799, Aug 2014. [Online]. Available: http://opg.optica.org/ol/abstract.cfm?URI=ol-39-16-4796

[7] J. Huber, A. Ambs, and J. Wöllenstein, "Miniaturized photoacoustic carbon dioxide sensor with integrated temperature compensation for room climate monitoring," *Procedia Engineering*, vol. 120, pp. 283–288, 2015, eurosensors 2015. [Online]. Available: https://www.sciencedirect.com/science/article/pii/S1877705815022791

[8] L. Xiong, W. Bai, F. Chen, X. Zhao, F. Yu, and G. J. Diebold, "Photoacoustic trace detection of gases at the parts-per-quadrillion level with a moving optical grating," *Proceedings of the National Academy of Sciences*, vol. 114, no. 28, pp. 7246–7249, 2017. [Online]. Available: https://www.pnas.org/doi/abs/10.1073/pnas.1706040114

[9] R. Bauer, T. Legg, D. Mitchell, G. M. H. Flockhart, G. Stewart, W. Johnstone, and M. Lengden, "Miniaturized photoacoustic trace gas sensing using a raman fiber amplifier," *Journal of Lightwave Technology*, vol. 33, no. 18, pp. 3773–3780, 2015.

[10] S. Li, Q. Yu, Z. Chen, and J. Lin, "Sensitive intracavity photoacoustic spectrometer based on CO2 waveguide laser," in *Instruments for Optics and Optoelectronic Inspection and Control*, G. H. Wei and S. Liu, Eds., vol. 4223, International Society for Optics and Photonics. SPIE, 2000, pp. 145 – 148. [Online]. Available: https://doi.org/10.1117/12.401777

[11] Z. Wang, Q. Wang, W. Zhang, H. Wei, Y. Li, and W. Ren, "Ultrasensitive photoacoustic detection in a high-finesse cavity with pound–drever–hall locking," *Opt. Lett.*, vol. 44, no. 8, pp. 1924–1927, Apr 2019. [Online]. Available: http://opg.optica.org/ol/abstract.cfm?URI=ol-44-8-1924

[12] A. Miklos, P. Hess, and Z. Bozoki, "Application of acoustic resonators in photoacoustic trace gas analysis and metrology," *Review of Scientific Instruments*, vol. 72, no. 4, pp. 1937–1955, 2001.

[13] M. Ilke, R. Bauer, and M. Lengden, "A calibration-free methodology for resonantly enhanced photoacoustic spectroscopy using quantum cascade lasers," *IEEE Sensors Journal*, vol. 20, no. 18, pp. 10 530–10 538, 2020.

[14] J. R. P. Bain, W. Johnstone, K. Ruxton, G. Stewart, M. Lengden, and K. Duffin, "Recovery of absolute gas absorption line shapes using tunable diode laser spectroscopy with wavelength modulation—part 2: Experimental investigation," *Journal of Lightwave Technology*, vol. 29, no. 7, pp. 987–996, 2011.

[15] G. Zhang, K. Chen, M. Guo, C. Li, L. Xu, N. Wang, and X. Zhao, "Miniature 3d-printed resonant photoacoustic cell for flowing gas detection," *Sensors and Actuators A: Physical*, vol. 341, p. 113594, 2022. [Online]. Available: https://www.sciencedirect.com/science/article/pii/S0924424722002321

[16] Y. He, Y. Ma, Y. Tong, X. Yu, and F. K. Tittel, "Hcn ppt-level detection based on a qepas sensor with amplified laser and a miniaturized 3d-printed photoacoustic detection channel," *Opt. Express*, vol. 26, no. 8, pp. 9666–9675, Apr 2018. [Online]. Available: https://opg.optica.org/oe/abstract.cfm?URI=oe-26-8-9666

[17] M.-S. Niu and L.-K. Song, "A 3d-printed microresonator based on the quartz-enhanced photoacoustic spectroscopy sensor for methane detection," *Journal of Applied Spectroscopy*, vol. 85, pp. 786–790, 2018.

[18] T. Rück, R. Bierl, and F.-M. Matysik, "Low-cost photoacoustic no2 trace gas monitoring at the pptv-level," *Sensors and Actuators A: Physical*, vol. 263, pp. 501–509, 2017. [Online]. Available: https://www.sciencedirect.com/science/article/pii/S0924424717304843

Utkarsh Dwivedi received his B.Eng (Honours) degree in Electronic and Electrical Engineering from the University of Strathclyde in 2017.

He is a PhD student at the University of Strathclyde investigating application of 3-D printed photoacoustic and non-dispersive infrared sensors for detection of methane in cattle farms.

Mark Donnachie received the M.Sci. degree in physics from the University of Dundee in 2018. He joined the Centre for Microsystems and Photonics at the University of Strathclyde, Glasgow, U.K., in 2018 as a Ph.D. student, where his research involves the development of a MEMS and fibre optic enabled multimodal microscope. He is also currently working as a research assistant in laser-based gas sensing applications in the Centre for Microsystems and Photonics at the University of Strathclyde, Glasgow, U.K.

Metin Ilke received his M.Sc degree in Optical Technologies and a Ph.D. degree from the University of Strathclyde, Glasgow, U.K., in 2016 and 2022. His PhD research focused on the use of 3D-printed photoacoustic spectroscopy techniques for the control of various industrial processes.

Ralf Bauer received his Dipl.-Ing. degree in Mechatronics from the University of Erlangen-Nuremberg, Germany in 2010 and his Ph.D from the Department of Electronic and Electrical Engineering at the University of Strathclyde, Glasgow, U.K. in 2013.

He is currently a Senior Lecturer in the Department of Electronic and Electrical Engineering at the University of Strathclyde, Glasgow. His research interests are in the field of MEMS enabled sensors and systems focusing on areas of biomedical sensors, optical sensors, microscopy development and biomedical imaging systems.

Michael Lengden received the M.Phys. degree and Ph.D. from the Department of Physics at the University of Manchester, Manchester, UK in 2001 and 2006 respectively.

He was an Applications Engineer at the Laboratory Impex Systems, Ltd from 2006-2007. In 2007 he joined the Centre for Microsystems and Photonincs in the EEE department at the University of Strathclyde, Glasgow, U.K. as a Research Fellow, and is now a Reader in the same department. He is engaged in research into high-temperature and high-pressure gas composition measurements using tunable diode laser spectroscopy for harsh environments, such as aero-engine exhausts, mid-pressure liquid fuel combustion rigs, and solid oxide fuel cells.